



CHARACTERISTICS AND THERMAL PERFORMANCE OF NANOFLUID FILM OVER HORIZONTAL MULTI-FACETED CYLINDER

Fithry Mohd Amir*, Mohd Zamri Yusoff, Saiful Hasmady Abu Hassan

College of Engineering, Universiti Tenaga Nasional (UNITEN), Jalan IKRAM-UNITEN, 43000, Kajang, Selangor, Malaysia

ABSTRACT

Nanofluid film on a horizontal tube is investigated numerically on the circular and multi-faceted cylinder. The fluid flow characteristics, including film thickness, shear stress, and thermal performance, are observed and analyzed. Fluid film on the circular surface is typical in many engineering applications, but the study of nanofluid film on non-circular surface is deficient in literature. The study provides a numerical model of a multi-faceted cylinder to simulate the nanofluid film on the non-circular surfaces using a volume of fluid (VOF) method. The ratio of Brownian motion to thermophoretic diffusion, N_{BT} developed along the film thickness in phases, in which the dominant phase, the steady-state N_{BT} phase, can be used as the average N_{BT} . Although, in general, the heat transfer performance of Alumina and Titania is better than water, producing higher HTC and Nu on both cylinders, Water, however, displays significant improvement relative to the base thermal performance of water fluid film on the circular cylinder.

Keywords: *Falling film on tube; nanofluid film, Alumina, Titania, heat transfer coefficient; multi-shape, non-circular cylinder, multi-geometry, volume of fluid, horizontal tube, wall shear stress.*

1. INTRODUCTION

In recent years, the enhancement of thermal performance of heat exchanger machines such as refrigeration absorber and desalination evaporator has been quite challenging and more demanding as more energy efficient machines are required to save operating and maintenance cost.

Beyond the heat exchanger machines, nanofluid study progression has been made in non-Newtonian fluid which focuses on the characteristics of nanofluid on stretched sheet (Alkawasbeh et al. 2020) and internal flow with protruded ribbed (Singh et al. 2018). Nanofluid is likewise a prospect to power saving operation in heat exchanger machines particularly involving fluid film applications. The study of nanofluid in falling film application is also a testament to this development but it still has not reached extensive level. Prior work is limited to a subset of limited application such as refrigeration absorber involving vertical and round surfaces. It has been of interest for a significant period of time but the literature has not progressed so much, yet the potential is still very much significant.

Falling film on tube requires low charge refrigerant (J. Ruan et al. 2018) which is beneficial in producing optimized heat transfer. It also provides wide range of surface enhancement method such as superhydrophilic (Zheng et al. 2017), surface roughness to improve wettability (Bock, Meyer, and Thome 2019) and improved film spreading through capillary transport (Eichinger et al. 2018). The enhancement of heat transfer in falling film application can be further extended by using nanofluid.

In falling film with nanofluid, Turkyilmazoglu (2015) found that an increase in volume fraction reduces the film thickness which enhance the heat transfer. Turkyilmazoglu (2017) also learned that Ag (silver) performed the best while Titania the worst due to their thermal conductivities. Similar thermal performance was observed on curved surface. In general, by increasing nanoparticle concentration, heat

transfer was improved attributed to thinner fluid film according to Jani (2013). But the author use Alumina nanofluid and depending on the flow region, it was reported that the fully developed region contributed to most of the thermal enhancement. Even though the generalized assumption of increasing nanoparticle volume fraction and thermal conductivity of the nanofluid will lead to improved heat transfer, there are other parameters that should also be considered. In most experimental work in literature involving refrigeration absorber, parameters such as solution flow rate, viscosity and stability of the nanofluid were also observed which contribute significantly to heat transfer improvement of the nanofluid.

Common solutions used in combination with water in absorber include lithium bromide and ammonia. In lithium bromide (LiBr) solution, various nanoparticles were investigated including Copper Oxide, Copper (Cu), Fe, Carbon nanotube (CNT) and Fe_3O_4 which resulted in enhanced thermal performance. In investigation by Gao et al. (2020), nanoparticle copper oxide effect on falling film absorption of LiBr was of area of interest. The solution mass transfer flux, mass transfer rate and mass transfer coefficient increased as a result of copper oxide nanoparticles. The effect is most significant when the inlet temperature is high and concentration of solution is low. Ben Hamida et al. (2018) used Copper nanoparticles, observed that as volume fraction increased from 0% to 10%, the absorption performance was enhanced 15%. The enhanced performance was observed significantly at $Re=55$ and below. L. Zhang et al. (2018) also observed similar results with increasing solution flow rate and nanoparticles mass fraction. But the performance is highly dependent on nanoparticle size which decreases with increase particle size. The type of nanoparticles is also crucial as Cu nanoparticle found to best improve the performance according to the author. Kang et al. (2008) suggested that to solve the sedimentation issue, Fe and CNT are used. These nanoparticles are not only good candidate to resolve the sedimentation issue but able to provide good stability condition. But the improvement of the solution mass flow rate increment is more significant than increasing the nanoparticles concentration. L. Y. Zhang & Wang (2017) investigated with Fe_3O_4 nanoparticle. In which the key parameters

* Corresponding author. Email: fithrya@yahoo.com

studied were solution flow rate, nanoparticle concentration and size. The decrease in nanoparticle size increases the absorption rate of water vapor and solution concentration difference of inlet and outlet. The authors recommended Fe_3O_4 mass fraction of 0.05% with particle size of 20 nm to obtain mass transfer enhancement in the absorber process. Although in general the higher nanoparticle concentration contributes to increased heat transfer performance, changing the operating parameter such as mass flow rate is proven to produce more significant improvement. This suggests that many issues remain unexplored in the course of understanding the effect of nanoparticle on heat transfer performance, particularly the use of carbon nanotube and Fe nanoparticles.

However, B. Ruan & Jacobi (2012) used multi-wall carbon nanotube (MWCNT) in water and ethylene glycol (EG) based fluid and reported interesting results. The nanoparticle has caused the water based fluid to behave as Newtonian fluid while EG as non-newtonian fluid. The heat transfer of nanofluids were lower compared to base fluids. HTC of EG decreases with increased MWCNT concentration. HTC of water based decreased then increased with increasing MWCNT concentration. In base fluids of water and ethylene glycol, concentration of 0.05, 0.14 and 0.24 were used in the experiment. Thermal conductivity for water and EG base was enhanced by 9% with 0.24% nanoparticle concentration. In addition, Sharma et al. (2020) reports that the EG and water combination is likely to develop higher entropy generation in both laminar and turbulent regime. However, this is limited to flow in conduit. Nonetheless, it raises interest to investigate the fluid film application in light of exergy analysis, which could elucidate the mechanism of nanofluid that augments the heat transfer.

Ammonia solution in absorber application also received a lot of focus by introducing nanoparticles such as carbon black particles, Fe_2O_3 , ZnFeO_4 , mono silver (Ag), Copper, Copper oxide and Alumina. Li et al. (2015) observed an optimum point for mass fraction of the carbon black nanoparticles in order to obtain improvement in falling film generation rate. The sedimentation, solid-liquid separation and suspension aggregate issues is not observed using carbon black nanoparticles but the nanoparticle addition was found to enhance absorption process. Optimal mass fraction of nanoparticles is also crucial to obtain improved absorption performance as Yang et al. (2011) revealed. The enhancing effect of nanofluid outperforms enhancement of increase mass fraction of ammonia solution. 70% and 50% improvement in absorption ratio was obtained by using Fe_2O_3 and ZnFeO_4 , which is contrary to what L. Y. Zhang & Wang (2017) has learned by using lithium bromide as base solution with CNT and Fe nanoparticles.

Using 0.02% concentration of mono silver (Ag) nanoparticle, the absorption rate was improved by 55% in ammonia solution of falling film as Pang et al. (2012) found. The author attributed the mass transfer enhancement on enhanced heat transfer through faster mass diffusion in the bulk liquid from nanoparticle motion and breaking of the gas bubble. Cu, CuO and Al_2O_3 nanoparticles were used in the experiment in which the effective absorption performance was improved especially by Cu nanoparticle as found by Kim et al. (2006). But the experiment setup is not a complete falling film absorber. The bubble was generated using an orifice and observed by bubble behavior visualization equipment. Further study in actual setup is required to get more data under bubble mode. In a numerical investigation, Yang et al. (2014) shows that when the absorption pressure decreases, the relative intensity effect on absorption rate is lowered due to variation of thermal conductivity. The model also shows that the nanofluid viscosity has low effect on absorption performance. The author suggest that the model can be used for any nanoparticle.

Brownian motion is the random motion of nanoparticles and thermophoretic effect is a phenomenon in which particles diffusing under effect of temperature difference (Buongiorno 2006). The effect of Brownian motion and thermophoretic are approaches to observe the effect of nanoparticle in the base fluid. The work of Malvandi, Ganji, et al. (2016) is among the references for study involving particle migration. Malvandi, Ghasemi, et al. (2016) investigated the effect of nanoparticle

migration in nanofluid of film condensation over vertical plate. Brownian and thermophoretic effect were considered by using modified Buongiorno model. It was observed that increase in temperature different at the plate wall increases nanoparticle migration which augment heat transfer rate. Increasing nanoparticle diameter intensifies the migration. Alumina performs better cooling performance compared to Titania nanoparticle in water based nanofluid as shown by the author. Generally it was observed that nanoparticle migration moved towards the cold surface by thermophoresis mechanism, which is also shown by Malvandi, Ghasemi, et al. (2016). Cheng & Peng (2020) investigated the migration effect of nanoparticle of film condensation over vertical cylinder by using the modified Buongiorno model. The nanoparticles migrated toward the cold wall which increased the localized concentration in that vicinity. The migration of nanoparticles is increased with decreasing in Brownian and Thermophoretic diffusivity ratio. But according to Cheng & Peng (2020), the distribution of nanoparticle is uneven along the thickness of the film, based on investigation of the nanoparticle migration on wavy falling film over a vertical plate using the integral-boundary-layer (IBL) method. This is also attributed to the temperature difference. The effective thermal conductivity is affected by nanoparticle localized concentration which increases thermal conductivity locally. The particle migration was also observed to affect flow rate and viscosity. Heat transfer is also expected to improve with increasing particle concentration.

Many researchers also attempted to improve thermal performance by decreasing the surface and interfacial tension of the base fluid by adding surfactant in addition to nanoparticle. Wide range of fluid film characteristics can be observed using this method which enhance our understanding of the effect of nanoparticle and surfactant on base fluid. Wen et al. (2018) used MWCNT (multi-walled carbon nanotube) particle and the surfactant polyvinyl pyrrolidone (PVP) at high speed agitation and ultrasonic vibration were utilized to obtain stable distribution of nanoparticle. In this investigation, the author observed that the nanofluid contact angle was reduced from 58.5° to 28° . The film thickness also reduced by approximately 0.1 mm. Wetting area was also increased by 21.5%. The thermal conductivity of the nanofluid with 0.1% nanoparticle has no significant change. The improvement in dehumidification rate of 26.1% and 25.9% for surfactant and nanoparticle respectively was contributed to the decrease in contact angle and improved wettability. B. Ruan et al. (2010) asserted that the improvement in dehumidification was attributed to the surfactant while the nanoparticle plays no significant role. B. Ruan et al. (2010) investigated with aluminum oxide in falling film on horizontal tube with particle concentration of 0%, 0.05%, 0.5%, 1% and 2% with Sodium dodecylbenzene sulfonate (SDBS) surfactant. No significant heat transfer improvement was observed. It was inferred that the cause of this might be that the thermal conductivity did not depart from the based fluid. Yang et al. (2010) used polyacrylic acid (PAA) and sodium dodecyl benzene (SDBS) surfactant with alumina nanoparticle. Absorption ratio was improved by 30% for combination of Alumina and PAA with ammonia solution initial concentration of 15% than using SDBS. B. Ruan & Jacobi (2011) asserted that the result of the investigation of Alumina with and without surfactant was not encouraging in terms of heat transfer enhancement. However, the flow transitional Reynold number increased by 20% with 2% nanoparticle concentration for water based nanofluid under all mode transition. The author did not offer any conclusive explanation citing that more research to understand this behavior. Lee (2009) used Arabic gum as a dispersion stabilizing agent and added to the lithium bromide solution. This combination reduced heat and mass transfer by 18% and 23% respectively. The high molecules produced by the Arabic gum addition was cited as reason for this which hinders nanoparticle movement. But by using 2-Ethyl-1-Hexanol surfactant alone with the nanoparticle, the heat and mass transfer were improved by 19% and 77% respectively. The surface tension was weakened by the surfactant, inducing Marangoni convection which improved heat and mass transfer.

Although in theory, the weakening of the surface tension may improve heat and mass transfer, not all surfactant will produce positive results. The combination of surfactant with nanoparticle will result in unexpected results and behavior of the nanofluid as found by B. Ruan, Jacobi, and Li (2010), Yang et al. (2010), B. Ruan and Jacobi (2011), and Lee (2009). In retrospect, the scope of combination of surfactant and nanofluid alone is lacking in literature, which provides great opportunity in understanding the performance of the surfactant in a broader range of engineering applications.

In this study, the numerical investigation of nanofluid film on horizontal multi-faceted tube will be presented. The combination of different geometry will provide different surfaces on similar fluid path. This is also one of the motivation of this study since the available literature focused on flat vertical and cylinder surface, the study will provide an opportunity to understand nanofluid kinematics on non-circular surfaces. Such condition can be encountered in cooling tower fill which essentially comprises of different fill arrangement.

The study will provide an understanding of the nanofluid film characteristics and thermal performance under different flow conditions and surfaces. The design of the multi-faceted cylinder is also a novelty which can also be applied on other falling film applications including refrigeration and desalination.

The literature involving nanofluid on such surface and falling film application is still not extensively addressed and this study aims to investigate the effect of nanofluid on parameters that can improve thermal performance. Turkyilmazoglu (2017) and Jani (2013) were able to show that the film thickness is affected by the nanoparticle concentration on flat and curved surfaces. But the characteristics of the nanofluid with sharp edges is not available in existing literature to the best of the authors' knowledge and will be addressed in this study.

2. PHYSICAL MODEL

The multi-faceted cylinder considers three main surfaces: a half-round tube, vertical flat, and tilted flat surfaces. The dimensions of the multi-faceted cylinder are shown in Figure 1. The equivalent round cylinder is of the same perimeter as the multi-faceted cylinder with a diameter of $D=26.0234$ mm. Cylinders of the same perimeter enable comparison of the same heat transfer area.

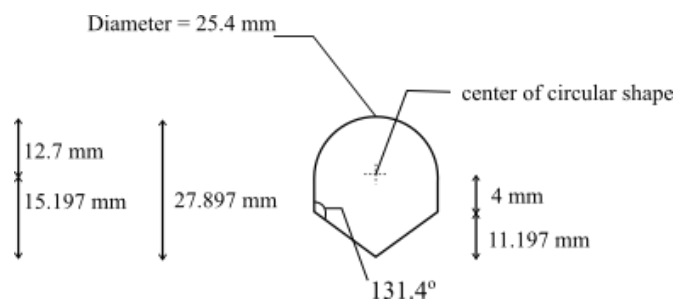


Fig. 1 Multi-faceted cylinder dimensions.

The fluid film location on the cylinders is reported by using the y-dimensionless location, as shown in Figure 2 and Figure 3. Y-dimensionless is the y distance ratio from the top over the total height, H of the respective cylinders. The fluid film will flow from $Y^*=0$ at the top to $Y^*=1$ to the bottom. The ranges of the three surfaces of the multi-faceted cylinder are $Y^*=0$ to 0.46, $Y^*=0.46$ to 0.60, and $Y^*=0.60$ to 1, representing the half-round, flat vertical, and tilted flat respectively.

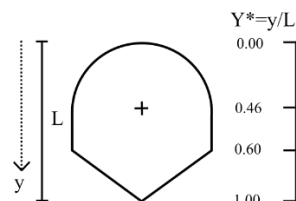


Fig. 2 Y^* dimensionless location on the multi-faceted cylinder

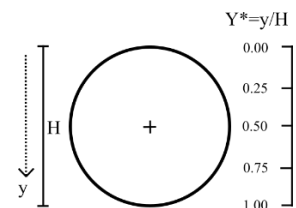


Fig. 3 Y^* dimensionless location on round cylinder

To characterize the thermal performance, two dimensionless temperatures are used. T_{wall}^* , the dimensionless wall temperature, identifies the surface with enhanced heat transfer augmentation. Second, to determine the thermal boundary layer, the dimensionless temperature, T^* , is calculated. The dimensionless film thickness, X^o , is illustrated in Figure 4.

$$X^o = \frac{X - X_1}{X_2 - X_1} \quad (1)$$

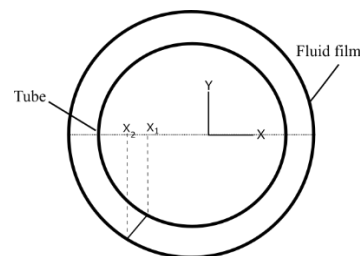


Fig. 4 Location along the fluid film in the normal direction is represented by dimensionless X^o .

3. NUMERICAL METHODOLOGY

The numerical model is created with the commercial software FLUENT from ANSYS. The laminar viscous model is used in this study. The falling fluid film is treated as an incompressible fluid flowing over the cylinder surface with a surface tension of 0.073 N/m (Zhao, Ji, He, et al. 2018) and gravity force. At a normal operating condition of 101,325 Pascal, the gaseous state is set to be air. The water inlet is located 5 mm above the cylinder and has a 2 mm opening. The simulation is performed on the symmetrical half of the cylinder. A constant wall heat flux of 47,300 Watt.m⁻² is applied on the wall.

3.1 Governing equations

The velocity of the fluid film at the inlet is calculated using the classical Reynolds number as followed:

$$Re = (\rho V D) / \mu \quad (2)$$

The film Reynolds number with the liquid load in the parameter in this study is defined as (Bock, Meyer, and Thome 2019) (Pu et al. 2019) (Jin et al. 2019),

$$Re = 4 \Gamma / \mu \quad (3)$$

In two-dimensional coordinates, the continuity expression is as follows:

$$\nabla V = 0 \quad (4)$$

The momentum equation of the mixture is

$$\frac{\partial}{\partial t}(\rho \mathbf{v}) + \nabla(\rho \mathbf{v} \mathbf{v}) = -\nabla p + \nabla[\mu(\nabla \mathbf{v} + \nabla \mathbf{v}^T)] + \rho \mathbf{g} + \mathbf{F} \quad (5)$$

The third term on the right-hand side represents the gravitational force, whereas the last term is the external body force or surface tension.

The surface tension is represented by the following expression, which is implemented through the Continuum Surface Stress (CSS),

$$\mathbf{F} = \nabla \bar{\mathbf{T}} \quad (6)$$

where

$$\bar{\mathbf{T}} = \text{surface stress tensor} \quad (7)$$

The energy equation for the mixture is expressed as follows,

$$\frac{\partial}{\partial t}(\rho C_p T) + \nabla \cdot (\rho C_p T \vec{v}) = \nabla \cdot \left(\frac{K}{C_p} \nabla C_p T \right) \quad (8)$$

For a fluid mixture, the volume of fluid (VOF) approach is used, which is a well-established method for tracking the interface of two immiscible liquids. The modified continuity equation below represents the distribution of the liquid phase in a two-phase flow with no mass transfer between the two phases. α_2 is the volume fraction of the secondary phase, which is the liquid phase.

$$\frac{\partial}{\partial t}(\alpha_2 \rho_2) + \nabla \cdot (\alpha_2 \rho_2 \vec{v}_2) = 0 \quad (9)$$

The α_1 which represents the volume fraction of the air phase, is computed by the following expression,

$$\alpha_1 + \alpha_2 = 1 \quad (10)$$

3.2 Nanofluid properties

The assumption of this study is that the nanoparticles are dispersed evenly within the base fluid which means the concentration is considered uniform. Well established classical formulas are used to calculate the effective physical properties of the nanofluid. The volume fraction, ϕ used in this study is 0.02. The following expressions are used to calculate the nanofluid physical properties:

The density is calculated based on Bock Choon Pak (2013) expression.

$$\rho_{nf} = (1 - \phi)\rho_f + \phi\rho_p \quad (11)$$

The thermal conductivity is approximated based on Maxwell-Garnett model (Oztop and Abu-Nada 2008).

$$\frac{k_{nf}}{k_f} = \frac{k_p + 2k_f - 2\phi(k_f - k_p)}{k_p + 2k_f + \phi(k_f - k_p)} \quad (12)$$

Xuan-Roetzel equation (Xuan and Roetzel 2000) is used to determine the specific heat capacity.

$$(\rho C_p)_{nf} = (1 - \phi)(\rho C_p)_f + \phi(\rho C_p)_p \quad (13)$$

There are several models available in literature to determine the dynamic viscosity, namely Wang et. al (1999) and Drew et. al (1999). Each models were developed under different assumptions. In this study the dynamic viscosity is calculated from work of Brinkman (Brinkman 1952) represented by Eq. (14) which is more generalized. Comparison of the various dynamic viscosity models applied and discrepancies in results was investigated by Duangthongsuk and Wongwises (2008). According to the authors, the low volume fraction will yield similar results of Nusselt and heat transfer coefficient using the various available models (Duangthongsuk and Wongwises 2008).

$$\mu_{nf} = \frac{\mu_f}{(1-\phi)^{2.5}} \quad (14)$$

The coefficients for Brownian motion and thermophoresis are calculated as:

$$D_B = \frac{k_B}{3\pi\mu_{bf}d_s} \quad (15)$$

$$D_T = \beta \frac{\mu_{bf}}{\rho_{bf}} \quad (16)$$

$$\beta = 0.26 \frac{k_{bf}}{2k_{bf} + k_s} \quad (17)$$

Where k_B is the Boltzmann constant and d_s is the nanoparticle diameter assumed to be 1×10^{-7} mm (Rashidi, Mahian, and Languri 2018). Thus, the parameter N_{BT} which is the ratio of the Brownian and the thermophoresis coefficients is determined by the following expression.

$$N_{BT} = \frac{D_B T_b^2}{D_T \theta} \quad (18)$$

In order to take into account, the operating temperature of the fluid in the investigation, the bulk temperature of the fluid is used and calculated as $T_b = (T_w + T_i)/2$. T_w is the average temperature on the wall and T_i is the fluid inlet temperature of 325 K. The local temperature of the fluid film is determined from $\theta = |T_w - T|$, where T is the fluid temperature at the boundary of gas-liquid interface, the same location the fluid thickness is calculated. Thus the parameter N_{BT} which is a non-dimensional variable will be used to investigate the extent of Brownian motion effect on the circular and multi-faceted surface (Buongiorno 2006). For $N_{BT} > 1$, the thermophoresis effect can be ignored and the Brownian motion is assumed to have dominant role. The N_{BT} is calculated along the length of the fluid thickness in the normal direction to the cylinder surface and represented by the dimensionless film thickness, X^0 .

Table 1 Thermophysical properties of nanoparticle and water

Nanoparticle/ Base fluid	Density, ρ	Thermal conductivity, k	Specific heat, C_p	Dynamic viscosity, μ
TiO ₂	4250	8.9538	686.2	-
Al ₂ O ₃	3970	40	765	-
Water	997.1	0.613	4179	0.000891

Table 2 Thermophysical properties of water-based nanofluid at $\phi = 0.02$

Nanofluid	Density, ρ	Thermal conductivity, k	Specific heat, C_p	Dynamic viscosity, μ
Al ₂ O ₃	1056.56	0.64882	3922.44	0.0009372
TiO ₂	1062.16	0.64364	3899.49	0.0009372

3.3 Mesh and discretization method

The semi-implicit method for pressure linked equations was used to solve the pressure coupling (SIMPLE). The compressive volume fraction is used to determine the fluid film's free surface location. To discretize the pressure, the body force weighted scheme is used. The first-order upwind scheme is used to solve the energy and momentum problems. The model is a multiphase system with air and water as the primary components.

Figure 5 presents the mesh of the solution on the circular cylinder. The grid is refined near the cylinder wall to obtain more accurate results of film thickness.

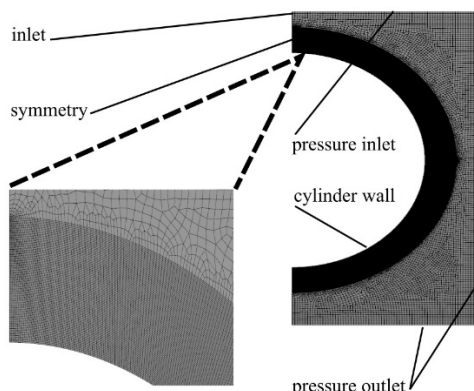


Fig. 5 The boundary and calculation domain on the circular cylinder.

3.4 Mesh independence analysis

Three simulations are performed to provide grid sensitivity analysis. A water liquid load of $\Gamma = 0.168 \text{ kg}\cdot\text{m}^{-1}\cdot\text{s}^{-1}$, a liquid feeder height of 5 mm, and a cylinder diameter of 25.4 mm are used, with grids of 70×500 , 90×500 , and 100×500 concentrated radially along the cylinder surface. Figure 6 depicts the film thickness of these simulations. Each grid system agrees with one another with only a minor difference near the cylinder's bottom. In this study, the grid 90×500 was chosen and used.

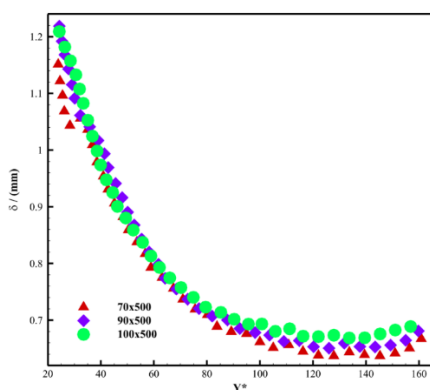


Fig. 6 Film thickness of various grid ($\Gamma = 0.168 \text{ kg}\cdot\text{m}^{-1}\cdot\text{s}^{-1}$, $H_f = 5 \text{ mm}$, $D = 25.4 \text{ mm}$)

3.5 Model validation

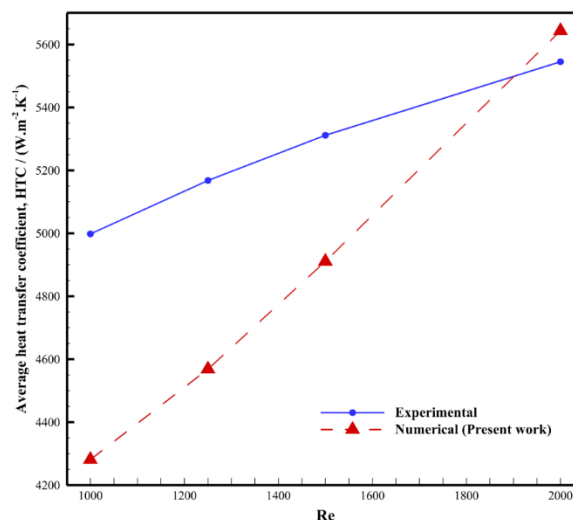


Fig. 7 Average heat transfer coefficient of 25.4 mm diameter round tube based on the experimental work of Parken et al. (1990) and numerical results versus Reynolds number.

Figure 7 depicts the average heat transfer coefficient of a circular tube obtained from experimental work by Parken et al. (1990) and numerical simulation. Heat transfer via falling film evaporation was experimentally investigated in his/her work. For both boiling and non-boiling conditions, different feed water temperatures were used. The water inlet is located 6.3 mm above the horizontal tube's 25.4 mm diameter. The experiments yielded correlation which is used to calculate the average heat transfer coefficient, which the current study validated the numerical results. The heat transfer coefficient increases as the Reynolds number increases, which is consistent with experimental values. The solution percentage error is less than 15% and steadily decreasing, approaching $Re = 2000$. The physics of increasing average heat transfer with increasing Re is acceptable for the study. Although the percentage error is less than 15%, the results are presented relative to the round tube, which is satisfactory for this study.

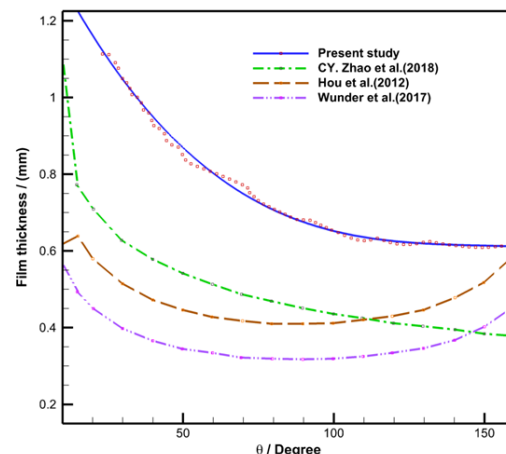


Fig. 8 Comparison of the film thickness in this present study and literature. (Zhao, Ji, Jin, et al. 2018) (Hou et al. 2012) (Wunder, Enders, and Semiat 2017)

To predict the thickness of a fluid film over a horizontal tube, several models have been developed. Zhao, Ji, Jin, et al. (2018) used explicit VOF to develop the correlation as a result of regression analysis that included the effect of Re , We , and Ar numbers. In comparison to the current study's direct film thickness extraction (Figure 8), the first-order

momentum solution over-predicts the solution The physics of the current study's film thickness, on the other hand, is similar to that of Zhao, Ji, Jin, et al. (2018), in which the thickness decreases as the angular location increases. This study obtained the fluid thickness data along the 0.99 VOF boundary, whereas previous studies only used data at a particular angular location.

4. RESULTS AND DISCUSSION

In this section, the main findings are presented, and the key findings will be highlighted. The numerical solution is conducted for constant wall heat flux for both horizontal cylinders under Reynolds number 1000, 1250, 1500, and 2000. Water and nanofluid with Alumina (Al_2O_3) and Titania (TiO_2) nanoparticles in water-based fluid are used to investigate their thermal performance and fluid characteristics on non-circular and circular surfaces represented by the multi-faceted cylinder and circular cylinder respectively.

4.1 Characteristics of nanofluid film thickness on multi-faceted cylinder

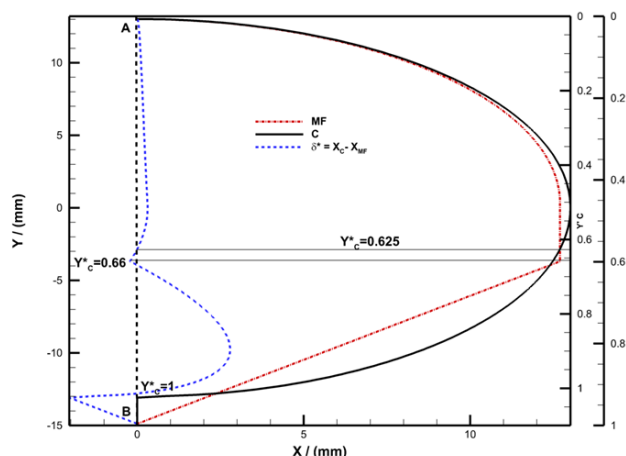


Fig. 9 Dimensions of the circular (C) and multi-faceted (MF) tube and respective Y^* . $X = 0$ indicates the symmetrical line of the tube. $\delta^* = X_C - X_{MF}$, indicated by the dashed blue line.

Figure 9 presents the actual dimension of the circular and multi-faceted cylinder. Although the tubes have a similar perimeter, their overall shapes, however, have sectional differences in dimension. In order to observe the locations of the surfaces on the tubes, the dimensionless Y^* is used.

On the Y -axis on the left, the Y^* of the circular and multi-faceted tube is provided. Since the height of the multi-faceted tube is slightly larger than the circular cylinder, the Y_{MF}^* scale is longer. The circular and multi-faceted relative to the x -axis between the two cylinders is $\delta^* = X_C - X_{MF}$, indicated by the dashed blue line. The vertical line A-B is located at $X=0$.

When the dashed blue line is in the positive region of the A-B vertical line, the circular cylinder is larger than the multi-faceted cylinder relative to the x -axis. This enables us to identify the key surface at Y^* based on surface change.

Thus, according to δ^* , on the circular Y^* scale, the circular cylinder is larger for the most part, but at $Y_C^*=0$ to $Y_C^*=0.625$, the change is not that significant. At $Y_C^*=0.66$, the multi-faceted cylinder is larger where the lower sharp edge of the vertical flat surface is located indicated by the δ^* in the negative region. The circular cylinder experiences the most significant δ^* at approximately $Y_C^*=0.66$ to $Y_C^*=1$.

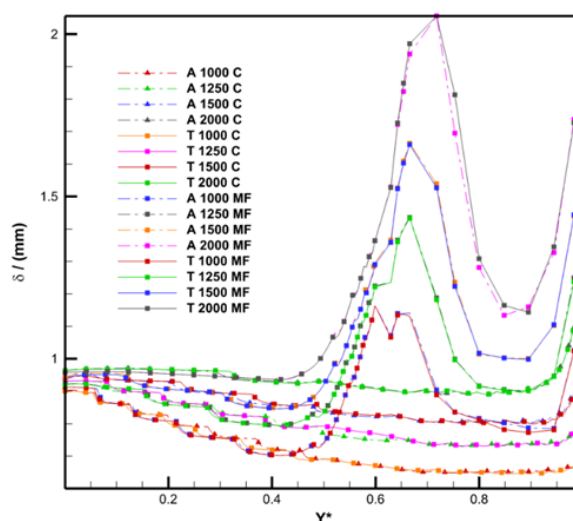


Fig. 10 Film thickness of Alumina(A) and Titania(T) on the circular(C) and multi-faceted (MF) cylinder at various Re versus Y^*

Figure 10 shows that the multi-faceted cylinder produces higher fluid thickness at approximately $0.4 < Y^* < 1$, which are located on the vertical and tilted flat surface component of the multi-faceted cylinder. The fluid thickness is not clearly distinguishable between TiO_2 and Al_2O_3 in which case it can be considered similar.

According to δ^* , the shape difference from $Y^*=0$ to $Y^*=0.5$ indicating small surface change. But based on Figure 9, the fluid thickness of the circular cylinder is slightly higher than multi-faceted cylinder within this range. This observation suggests that even a slight changes in the circular diameter can greatly affect the fluid thickness. The higher δ^* slightly after $Y^*=0.6$ however does not greatly impact fluid thickness as the flow is progressing into final section of the bottom half of both cylinders.

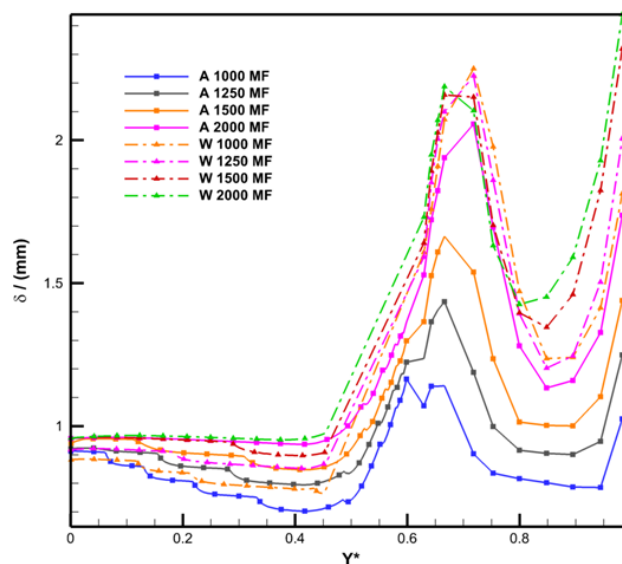


Fig. 11 Film thickness of Alumina(A) and Water(W) on the circular(C) and multi-faceted (MF) cylinder at various Re versus Y^*

The significant difference in fluid film thickness between water and Alumina can be observed on the multi-faceted cylinder, particularly at the vertical and tilted flat surfaces. According to Figure 11, between $0.4 < Y^* < 0.6$, the film thickness increases drastically by almost 50% and 100% by Alumina and water, respectively. Beyond $Y^* > 0.6$, all fluid flow reduces but is still larger than that produced on the circular surface

component on the top half of the cylinder. Between $0.4 < Y^* < 0.8$, Alumina shows greater increment than water in which within the same Y^* range, water does not show a significant difference in film thickness with increasing Re.

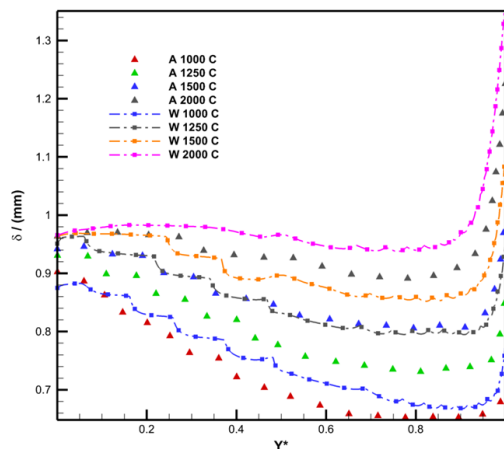


Fig. 12 Film thickness of Alumina(A) and Water(W) on the circular(C) cylinder at various Re versus Y^*

Figure 12 highlights the fluid thickness of Alumina and water on the circular cylinder. It is clear that with increasing Reynolds number, water produced higher fluid thickness compared to the nanofluid. The film thickness for all fluid flow at all Re decreases with decreasing Y^* . This is also an affirmation which according to Jani (2013), heat transfer is improved due to thinner fluid film by nanofluid.

4.2 Characteristics of nanofluid shear stress on multi-faceted cylinder

The wall shear stress is of significant interest in this study because it indirectly reveals the degree of motion of the fluid film. It determines the time rate of strain of the fluid film or, in other word, the fluid film velocity normal to the wall. The time rate of strain is directly proportional to the shear stress as per following expression, which represents the shear stress of a liquid near a wall,

$$\tau = \mu \frac{dv}{dy} \quad (19)$$

The shear stress is determined by the viscosity, and the strain time rate $\frac{dv}{dy}$, which also represents the velocity gradient normal to the wall. In this study, the wall shear stress is dependent on the time rate of strain or the velocity gradient, assuming the liquid viscosity is constant.

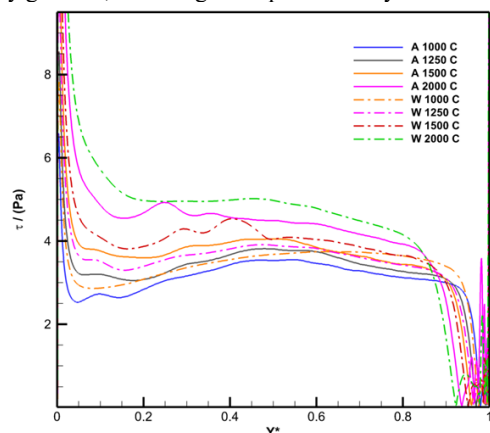


Fig. 13 Wall shear stress of Alumina (A) and Water(W) on the circular(C) cylinder at various Re versus Y^*

Figure 13 shows the wall shear stress of Alumina and Water on the circular cylinder at various Re. Water fluid film produces relatively higher shear stress than Alumina with increasing Re. The shear stress starts very high at the inlet at $Y^*=0$ and decreases at $Y^*=0.2$. It then stabilizes before increasing slightly at $Y^*=0.5$ before decreasing towards the bottom of the circular cylinder. Excluding the shear stress at the inlet, the peak shear stress is located at $Y^*=0.5$, which is at the center of the circular cylinder surface.

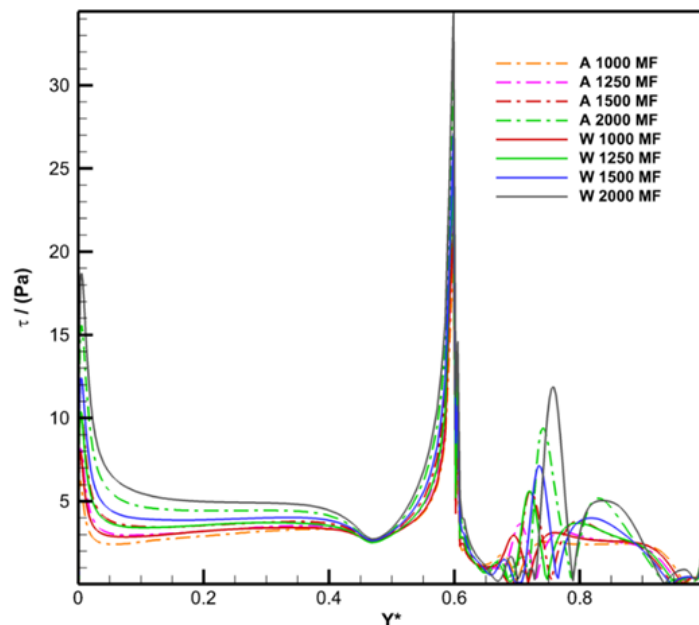


Fig. 14 Wall shear stress of Alumina (A) and Water (W) on the multi-faceted (MF) cylinder at various Re versus Y^*

Figure 14 presents the shear stress of water and Alumina on the multi-faceted cylinder. Water produced higher shear stress similar to that on the circular cylinder. The shear stress pattern is also quite similar with the fluid flow on the circular cylinder from $Y^*=0$ to $Y^*=0.4$, representing the circular surface component of the multi-faceted cylinder. As the fluid film travels down the vertical flat surface at $Y^*=0.4$ to $Y^*=0.6$, the shear stress increases drastically. At the precise location of $Y^*=0.4$ and $Y^*=0.6$, where there are sharp edges indicating surface changes, the fluid film will experience a drop in shear stress as it travels on a different surface.

The shear stress on the multi-faceted cylinder is relatively higher than the circular cylinder. The larger surface of the circular cylinder relative to the x-axis according to the δ^* at $Y^*=0$ to $Y^*=0.5$ suggests that a larger cylinder diameter will result in lower shear stress. The even larger δ^* at $Y^*=0.6$ to $Y^*=0.9$ increases the shear stress on multi-faceted cylinder. This surface location is represented by the tilted flat section of the multi-faceted cylinder and the bottom half of the circular cylinder.

The optimum film thickness slightly after $Y^*=0.6$ indicates that the fluid is accumulating at the particular region. Combined with an increase in velocity and capitalizing from the gravity force from $Y^*=0.4$ to $Y^*=0.6$, the fluid moves into a different surface area at the trailing edge of the vertical flat surface. The maximum shear stress is located near this vicinity, at $Y^*=0.6$. As the fluid passes the sharp edge at the trailing edge of the vertical flat surface, the surface change causes the fluid to accumulate, giving rise to optimum fluid thickness. Accordingly, the shear stress is also at the lowest value at this point, indicating that the accumulation process has resulted in reduced velocity, which is contributed by the flow separation (Figure 15).

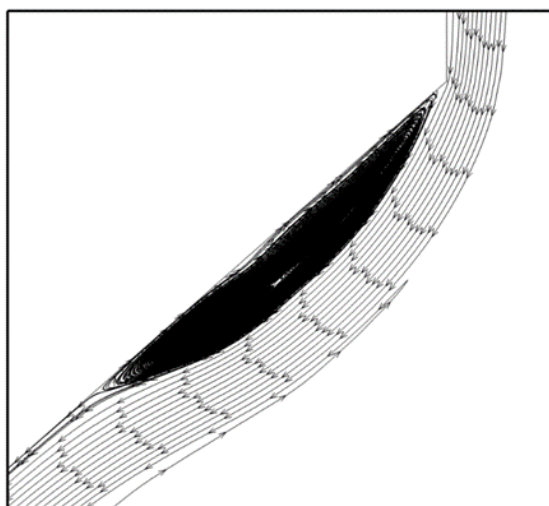


Fig. 15 The streamline of alumina fluid film on the tilted surface of the multi-faceted cylinder at $Re=1500$ shows flow separation at the location of maximum fluid thickness formation at approximately $Y^*=0.68$.

4.3 Brownian motion on the cylinder surface

In this study, the $N_{BT} > 1$ indicates that the Brownian diffusivity is dominant in the fluid flow compared to thermophoresis. Although the Brownian motion is generally dominant in the fluid film, the motion's intensity depends on a multitude of factors, such as wall temperature, shear stress, fluid temperature & velocity, and cylinder surfaces. The N_{BT} thus shows different characteristics on the multi-faceted and circular cylinder, which will be highlighted in this section.

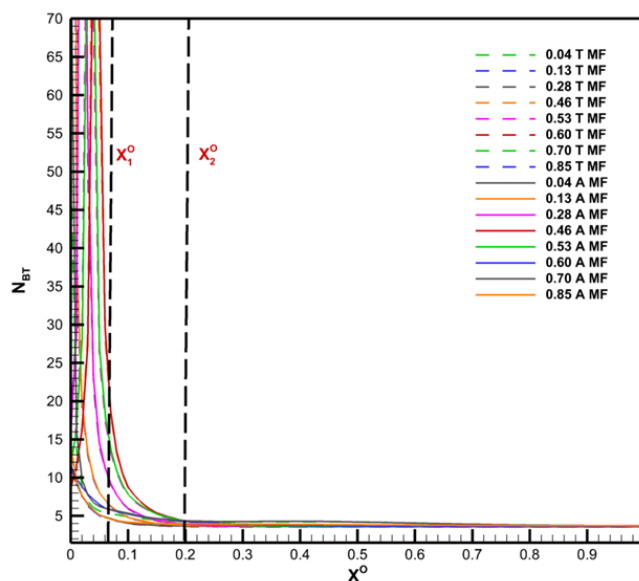


Fig. 17 N_{BT} of Alumina (A) and Titania (T) on the multi-faceted (MF) cylinder at various Re versus X^O

Figure 17 shows the N_{BT} on the multi-faceted cylinder at various Y^* . The optimum phase is located at a similar X^O as the circular cylinder. The transition phase, however, is at a lower region than the circular cylinder at approximately $X^O=0.2$. This observation suggests that the N_{BT} of the fluid film on the multi-faceted cylinder reaches its steady-state condition closer to the cylinder wall than the circular cylinder at $Re=2000$.

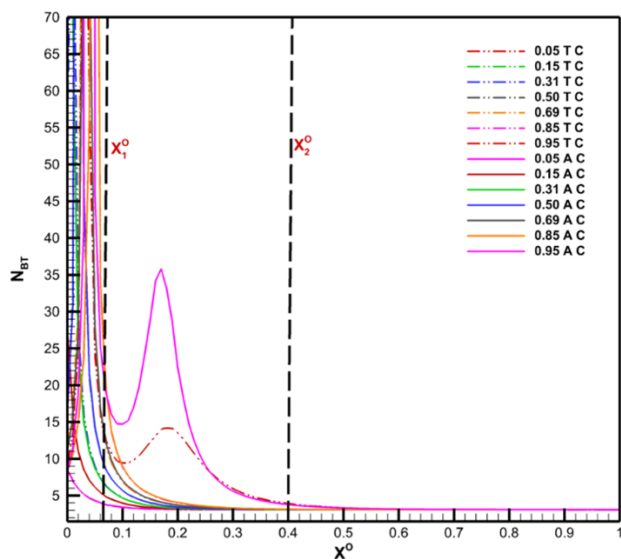


Fig. 16 N_{BT} of Alumina (A) and Titania (T) on the circular (C) cylinder at various Re versus X^O

The N_{BT} is classified into three phases in this study. The maximum N_{BT} is located at approximately $0 < X_1^O < 0.06$, which is considered to be in the optimum N_{BT} phase. The N_{BT} moves into the transition phase at $0.06 < X^O < 0.4$ and reaches its steady-state phase at $0.4 < X_2^O$ for the circular cylinder at $Re=2000$ (Figure 16). Generally, it is observed that the optimum N_{BT} phase is close to the cylinder wall. The region of the phases indicated by the area covered by X^O suggests that the steady-state region is dominant in the fluid film, followed by the transition and optimum phases region.

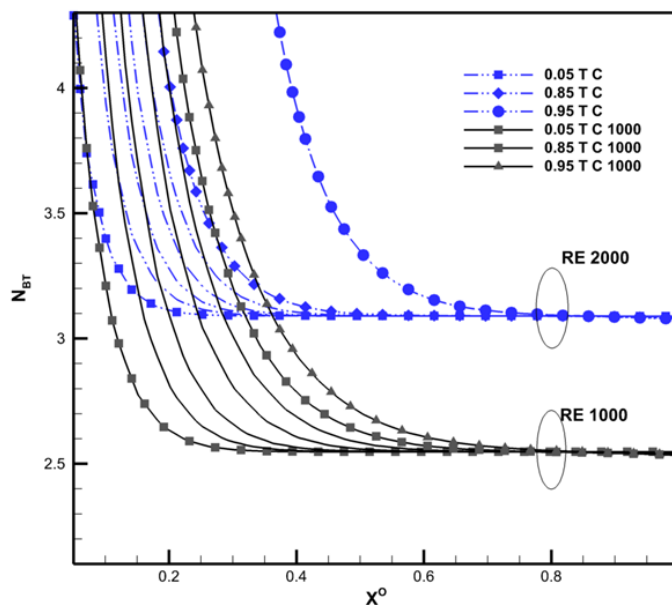


Fig. 18 N_{BT} of Titania (T) on the circular (C) cylinder at various $Re=1000$ and $Re=2000$ (Blue curve) versus X^O

Based on Figure 18, the region of optimum N_{BT} phase increases with increasing Re , indicating higher Brownian diffusivity along the film thickness on the circular cylinder. Nevertheless, this is not significant as the highest X^O at $Y^*=0.95$ for $Re=2000$ only occurs at the very bottom of the circular cylinder. Excluding this point, the optimum N_{BT} phase region decreases from $0.05 < Y^* < 0.85$ with increasing Re and Y^* . The steady-state N_{BT} phase increases with increasing Re .

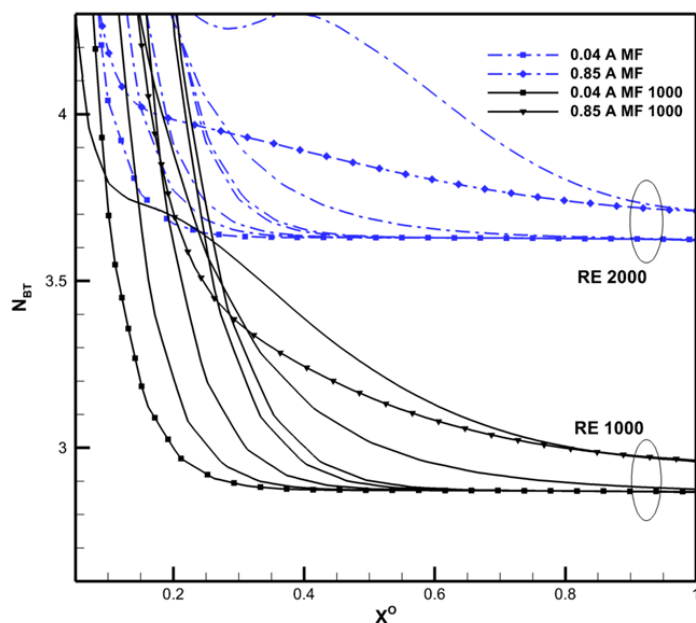


Fig. 19 N_{BT} of Alumina (A) on the multi-faceted (MF) cylinder at $Re=1000$ and $Re=2000$ (Blue curve) versus X^O

The steady-state N_{BT} phase is also increasing with Re on the multi-faceted cylinder (Figure 19). However, the optimum N_{BT} phase shows no significant change with increasing Re for the multi-faceted cylinder's circular component and vertical flat surface. However, the optimum N_{BT} phase on the tilted flat surface shows a decreasing trend with increasing Re , based on X^O at $Y^*=0.85$.

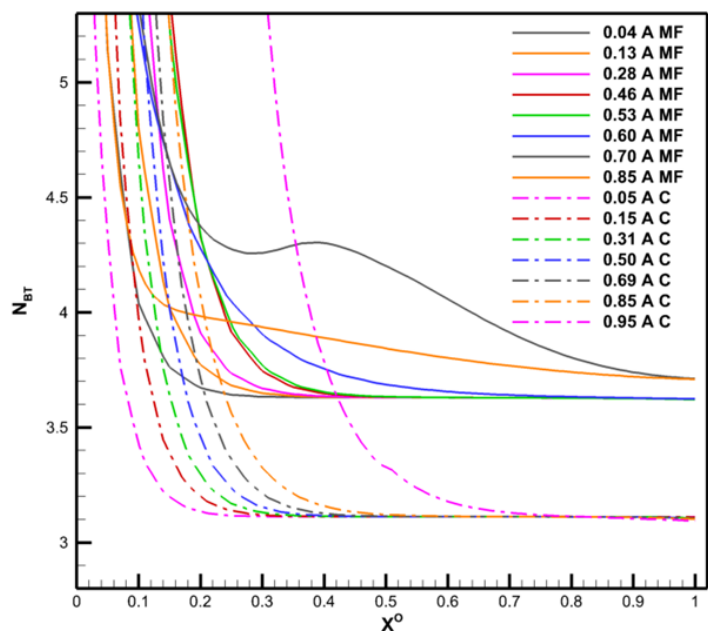


Fig. 20 N_{BT} of Alumina (A) on the circular(C) and multi-faceted (MF) cylinder at various $Re=2000$ versus X^O

The steady-state N_{BT} is relatively higher on the multi-faceted cylinder than the circular cylinder (Figure 20). Excluding the N_{BT} of the circular cylinder at $Y^*=0.95$, which is located near the bottom of the cylinder, the optimum N_{BT} phase shows no significant difference between the circular and multi-faceted cylinder.

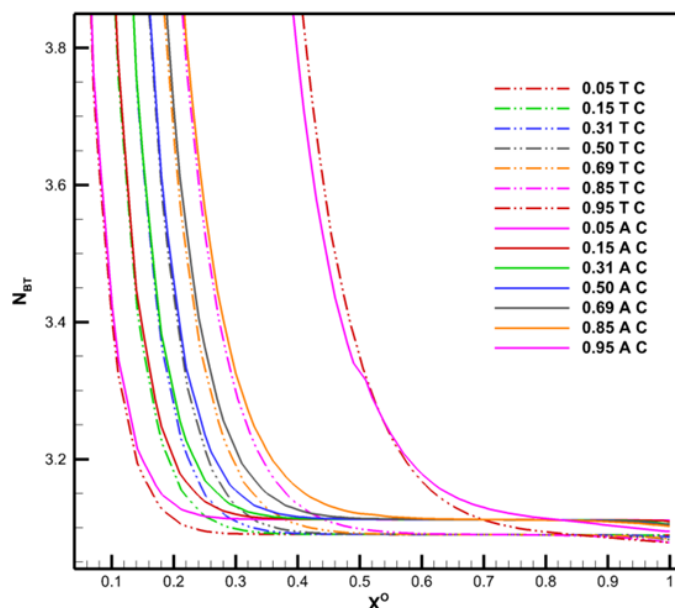


Fig. 21 N_{BT} of Alumina(A) and Titania(T) on the circular(C) cylinder at $Re=2000$ versus X^O

Figure 21 depicts the N_{BT} of Titania and Alumina on the circular cylinder at various Y^* locations. As the fluid film travels down on the circular cylinder surface, the optimum phase N_{BT} region increases almost uniformly before rising drastically at $Y^*=0.95$. The X^O on the circular cylinder is increasing with increasing Y^* , indicating the optimum phase N_{BT} is increasing along the film thickness, away from the cylinder wall.

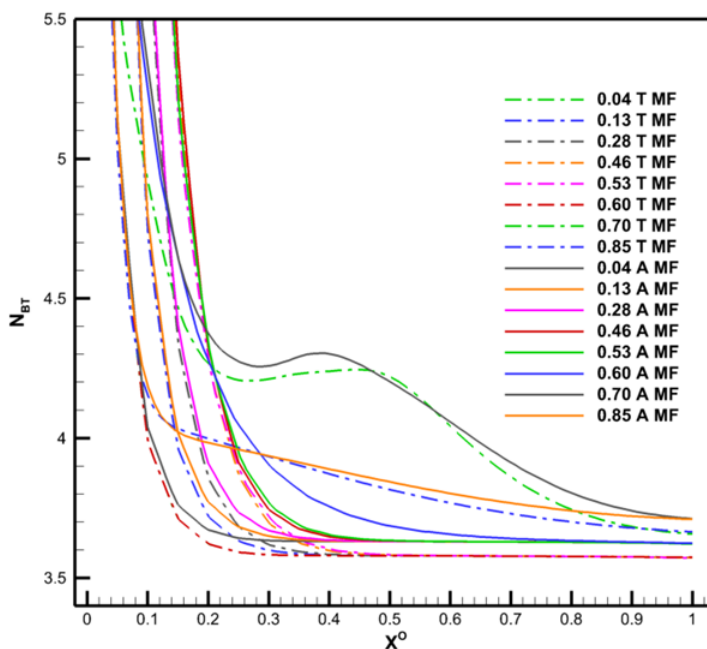


Fig. 22 N_{BT} of Alumina (A) and Titania(T) on the multi-faceted(MF) cylinder at $Re=2000$ versus X^O

A similar characteristic can be observed on the circular surface component of the multi-faceted cylinder from $0.04 < Y^* < 0.46$, which suggests that the optimum phase N_{BT} is moving away from the cylinder wall with rising X^O (Figure 22).

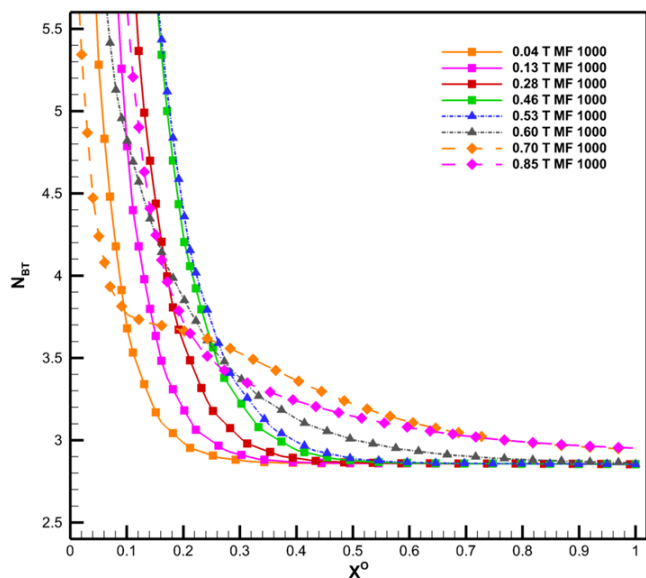


Fig. 23 N_{BT} of Titania(T) on the multi-faceted(MF) cylinder at $Re=1000$ versus X^O

N_{BT} on the multi-faceted cylinder behaves differently than on the circular cylinder because of fluid flow characteristics on its non-circular surfaces. Figure 23 represents the N_{BT} on the multi-faceted cylinder at different surfaces indicated by the various Y^* values. On the circular part of the cylinder at $0.04 < Y^* < 0.46$, X^O increases uniformly in the optimum and transition phase. However, as the fluid film travels down on the vertical flat surface at $0.53 < Y^* < 0.6$, X^O decreases. X^O further decreases in the optimum phase as the fluid film enters the leading edge of the flat tilted surface at $0.7 < Y^*$, and rises slightly as the fluid film travels to the bottom of the cylinder. However, X^O in the optimum phase never exceeds the maximum X^O produced on the circular surface component. This observation suggests that the region of optimum N_{BT} phase at the vertical and tilted flat surfaces moves closer to the cylinder wall, consequently increasing the steady-state N_{BT} phase region. The steady-state N_{BT} phase is slightly higher on the tilted flat surface than vertical flat and circular surfaces.

Cheng and Peng (2020) and Malvandi et al. (2016) presented their work focusing on particle migration of nanofluid film. According to Cheng and Peng (2020), an increase in nanoparticle concentration will enhance heat transfer. In this study, the nanoparticle concentration is constant; thus, the thermal augmentation on the cylinder is contributed by the properties of the nanofluid relative to water and the effect of the multi-faceted cylinder surface on the characteristics of the fluid film.

It is established that the wall shear stress is more significant on the multi-faceted cylinder, particularly contributed by the non-circular surfaces. When the velocity gradient normal to the wall increases, the Brownian motion is enhanced, ultimately compressing the nanoparticle close to the cylinder wall. The higher the wall shear stress, the smaller the region of the optimum N_{BT} phase. In other words, the region gets closer to the cylinder wall. This is supported by the observation in Figure 19 and 23.

4.4 Thermal performance of multi-faceted cylinder and circular cylinder

In this section, the thermal performance of the fluid film will be presented in three categories; dimensionless temperatures, the normalized Nusselt number, and the average heat transfer coefficient. The dimensionless temperatures will focus on the characterization of the thermal augmentation on the cylinder surfaces by the dimensionless wall temperature, T_{wall}^* , and the thermal boundary layer dimensionless temperature, T^* . The normalized Nusselt number will be presented by

normalizing the Nusselt number of the multi-faceted cylinder with the circular cylinder under the corresponding fluid.

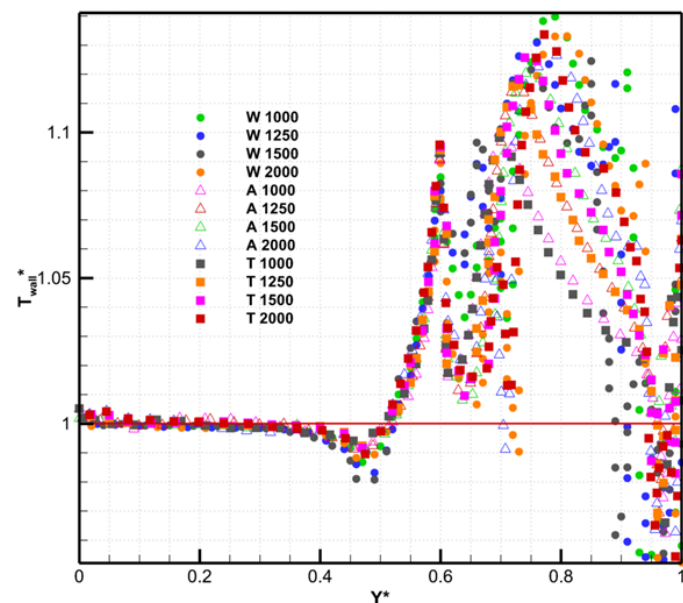


Fig. 24 Dimensionless wall temperature, T_{wall}^* of Alumina(A), Titania(T) and water(W) at various Re

$T_{wall}^* > 1$ means that the multi-faceted wall temperature is lower than the circular cylinder at the corresponding Y^* . This indicated that at similar Y^* location, the heat transfer is improved on the multi-faceted cylinder. The condition is vice versa when $T_{wall}^* < 1$. According to Figure 24, $T_{wall}^* > 1$ is significantly higher along $Y^* > 0.5$ on the multi-faceted cylinder. The thermal performance of the round cylinder shows a gradual and steady minuscule increase along the surface of the upper half of the cylinder between $0 < Y^* < 0.5$, after which the thermal performance of the circular cylinder begins to decrease. This observation reveals that most of the thermal augmentation on the multi-faceted cylinder occurs on the vertical and tilted flat surface. The thermal augmentation peaks at the vicinity of $Y^* = 0.8$, located at the midpoint of the tilted flat surface.

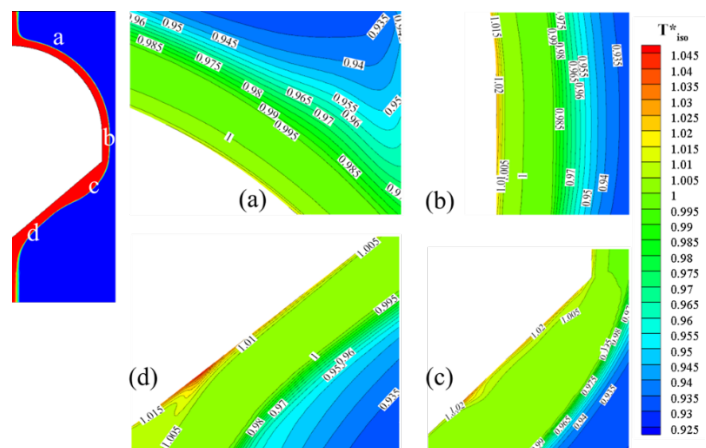


Fig. 25 Phase diagram of alumina on the multi-faceted tube at $Re=2000$ (Top left corner). The corresponding isotherms, T_{iso}^* by respective locations are denoted by a) circular surface, b) vertical flat surface, c) leading and d) trailing edge of tilted flat surface

T_{iso}^* denotes the temperature of the fluid film, which is non-dimensionalized by the fluid's T_{inlet} . T_{iso}^* indicates the local thermal distribution of the fluid film and hence does not offer the evaluation of

relative thermal performance in comparison to the circular and multi-faceted tube represented by T^*_{wall} .

The phase diagram and isotherms of the alumina on the multi-faceted tube are shown in Figure 25 at $Re=2000$. The region of high T^*_{iso} may be seen on the non-circular components of the multi-faceted tube's surfaces in Figure 25 (b), (c), and (d). In this regard, a greater T^*_{iso} indicates superior thermal performance. The T^*_{iso} on the circular surface in Figure 25 (a) is lower than on the other surfaces.

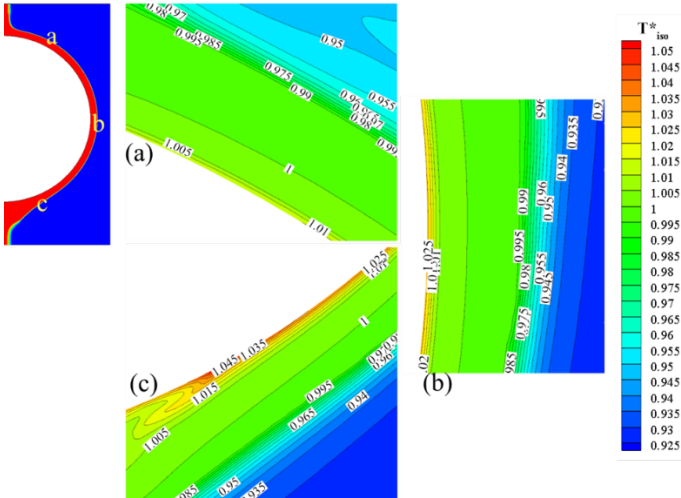


Fig. 26 Phase diagram of alumina on the circular cylinder at $Re=2000$ (Top left corner). The corresponding isotherms, T^*_{iso} by location are denoted by a) $Y^*=0.1$, b) $Y^*=0.5$, and c) $Y^*=0.95$

Figure 26 depicts the phase diagram and T^*_{iso} of alumina on the circular cylinder. Higher T^*_{iso} is observed near the lower half of the cylinder wall. This is also consistent with the observation on water fluid film on circular cylinder in our other work (Amir. Fithry, Zamri, and Hassan Saiful H. 2021). The nanofluid film displays similar trend of characteristics in T^*_{iso} as water fluid film on the circular and multi-faceted surfaces. Nevertheless, the thermal boundary layer is different due to different fluid thickness.

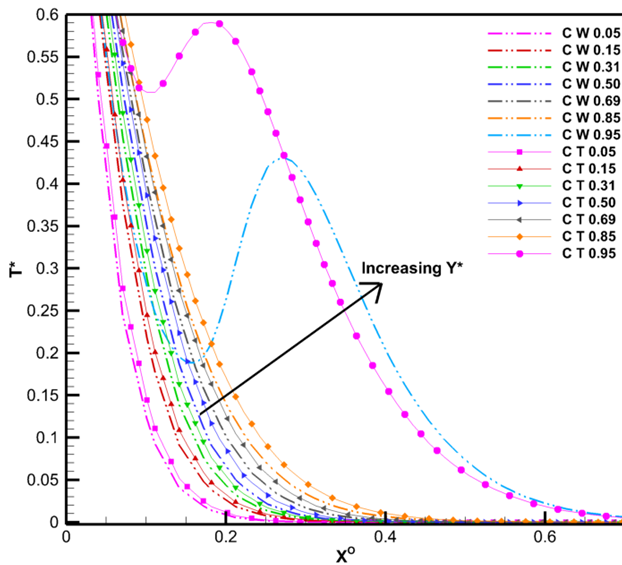


Fig. 27 Dimensionless temperature, T^* of Titania(T) and water(W) on the circular cylinder(C) at $Re=2000$ and various Y^* location

Figure 27 depicts the thermal boundary layer, T^* of Titania, and water on the circular cylinder. T^* decreases with increasing X^0 for all fluid

flow but T^* increases with increasing Y^* . T^* of Titania is slightly higher than water. In general, the local temperature decreases with increasing X^0 and reaches its lowest value at approximately $X^0=0.4$. In this case, a higher T^* indicates a better heat transfer performance because the cylinder wall is under constant wall heat flux. Although the fluid film thickness of water is generally higher than nanofluid, lower T^* of water suggests that the fluid thickness is not adequate compared to Titania which produces lower film thickness. This is contributed to the thermal properties of the nanofluid.

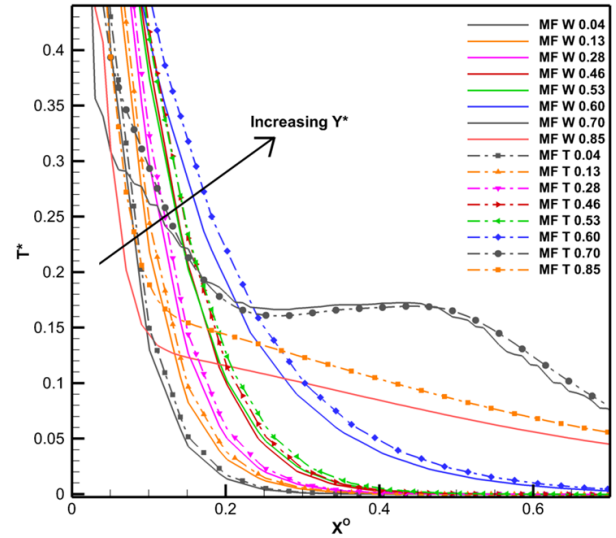


Fig. 28 Dimensionless temperature, T^* of Titania(T) and water(W) on the multi-faceted cylinder(MF) at $Re=2000$ and various Y^* location

In general, T^* shows the same increasing trend with Y^* and decreasing with X^0 on the circular component between $0.04 < Y^* < 0.46$ for all fluid flow, according to Figure 28. On the vertical flat surface at $0.53 < Y^* < 0.60$, T^* shows a significant rise with Y^* . Although T^* on the tilted flat surface at $0.7 < Y^* < 0.85$ is lower at lower X^0 , T^* increases drastically at $X^0=0.1$. The vertical and tilted flat surfaces also produce significantly higher T^* than the circular surface component in which $T^* > 0$ when it reaches $X^0=1$. Relatively, Titania has a higher T^* than water.

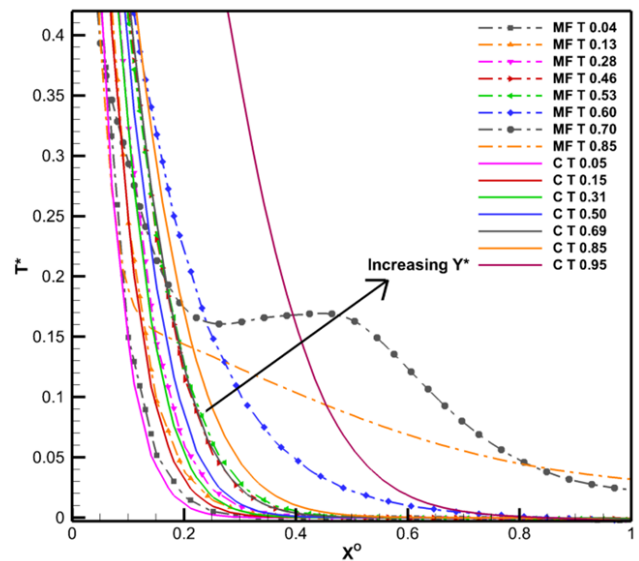


Fig. 29 Dimensionless temperature, T^* of Titania(T) on the circular(C) and multi-faceted cylinder(MF) at $Re=2000$ and various Y^* location

In general, T^* is relatively higher on the multi-faceted than the circular cylinder. Excluding T^* at $Y^*=0.95$ on the circular cylinder near the bottom, T^* reaches a steady state at approximately $X^0=0.4$ with $T^*=0$. T^* on the vertical and tilted flat surface on the multi-faceted cylinder, however, reaches $T^*=0$ at $X^0=0.8$ at the trailing edge of the vertical flat surface, while $T^*>0$ on the tilted flat surface (Figure 29). This suggests that the non-circular surfaces of the multi-faceted cylinder produce higher T^* , consequently enhancing heat transfer of the fluid film.

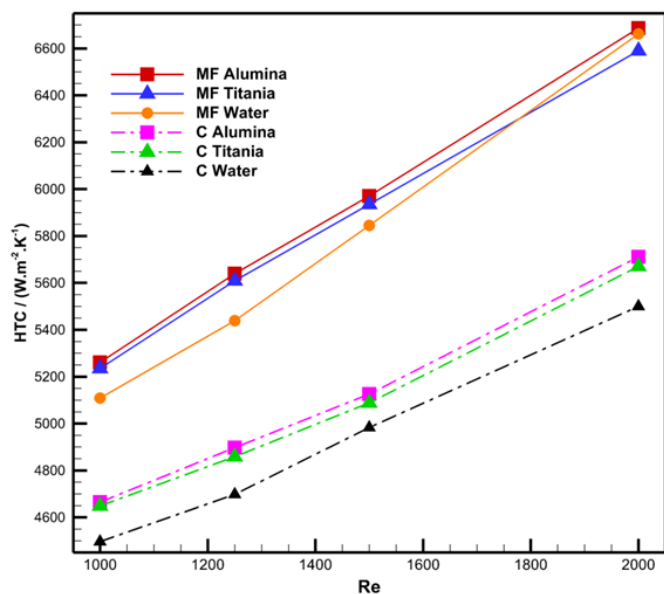


Fig. 30 Average heat transfer coefficient, HTC of Alumina(A), Titania(T), and Water(W) on the circular(C) and multi-faceted (MF) cylinder versus Re

Figure 30 illustrate the heat transfer coefficient, HTC of the nanofluids, and water on the circular and multi-faceted cylinder at various Re. The HTC is increasing with increasing Re for all fluid flow. The circular cylinder produced the lowest HTC with the lowest by water. The Alumina produces slightly higher HTC than Titania on the circular and multi-faceted cylinder, but not that significant. Water produces higher HTC than Titania at $Re=2000$. Generally, the highest HTC is produced by the multi-faceted cylinder with the highest by Alumina, Titania and water respectively.

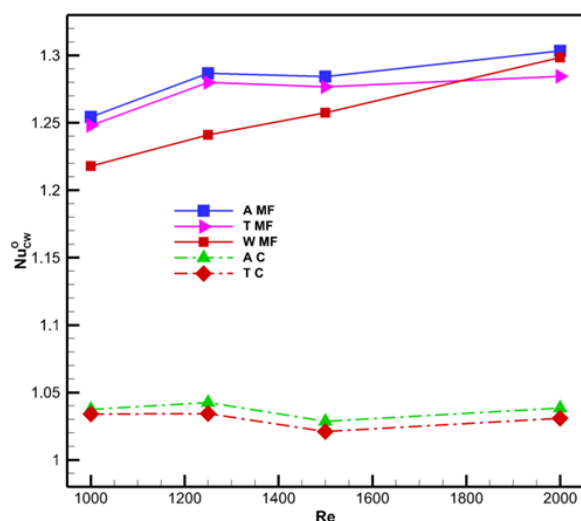


Fig. 31 Nu normalized to Nu of Water on the circular cylinder, Nu^0_{cw} , of Alumina(A), Titania(T), and Water(W) versus Re

Figure 31 illustrates the Nusselt number normalized to the Nusselt number of water fluid film on the circular cylinder, considering it produces the lowest HTC compared to fluid film on the multi-faceted cylinder and nanofluid. All types of fluid flow show thermal improvement relative to the water fluid film on the circular cylinder. Nanofluids on circular cylinder do not exhibit much improvement in this respect with increasing Re. The improvement is slightly decreased at $Re=1500$. A similar trend is observed by the nanofluid with the exception of Alumina, which shows considerable improvement at $Re=2000$. There is an approximately 2.5% increase of improvement by nanofluid compared to water on the multi-faceted cylinder at $1000 < Re < 1500$. Nevertheless, water shows almost a linear improvement at increasing Re with the highest improvement almost matching Nu^0 of Alumina at $Re=2000$.

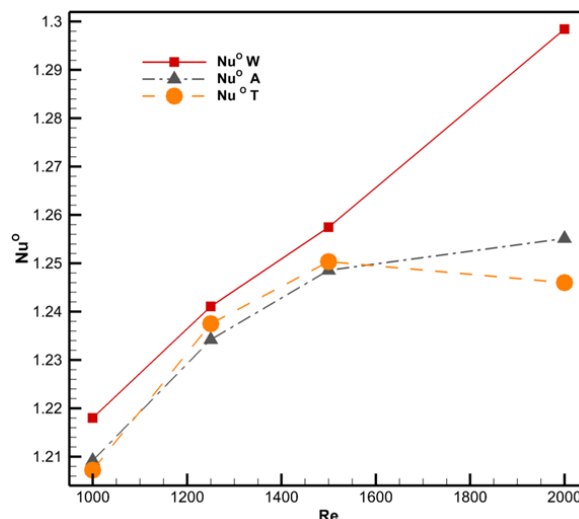


Fig. 32 Nu normalized to Nu of corresponding fluid on the circular cylinder, Nu^0 of Alumina(A), Titania(T), and Water(W) versus Re

Figure 32 illustrates the Nusselt number of fluid flows on the multi-faceted cylinder normalized with the Nusselt number of the corresponding fluid flow on the circular cylinder. Water shows a linear improvement of Nu^0 with increasing Re. However, nanofluid shows linear improvement at $1000 < Re < 1500$, but the Nu^0 drops for Titania at $Re=2000$, which indicates that the improvement achieved is less than achieved at lower Re. However, Alumina shows slight improvement at $Re=2000$. In this regard, all fluid flow shows significant advantages on the multi-faceted cylinder than the circular cylinder. However, the improvement is more significant in water, followed by Alumina and Titania, respectively.

5 CONCLUSIONS

The fluid film's thermal performance and dynamics over a multi-faceted horizontal cylinder have been investigated numerically and compared to its equivalent round cylinder by using water and nanofluid of Al and Ti_2O as nanoparticles. The improvement of thermal performance can be attributed to two factors in this study: the multi-faceted surface and the properties of the nanofluid.

Based on the results and discussion in the previous section, the following conclusions are made:

1. Even though water produces the maximum fluid film thickness on the multi-faceted cylinder, there is no significant rise with increasing Re at the non-circular surfaces. Titania and Alumina, however, show a significant increase in fluid film thickness on the non-circular surfaces with increasing Re. The increase of fluid

thickness at the non-circular surfaces is 50% and 100% for nanofluid and water, respectively.

2. N_{BT} on both cylinders can be classified into three phases: the optimum, transition, and steady-state N_{BT} phase. The steady-state N_{BT} phase increases on the multi-faceted cylinder. It gets closer to the cylinder wall than the circular cylinder. The steady-state N_{BT} increases with increasing Re and is higher on the multi-faceted cylinder. The steady-state N_{BT} can be used as the average N_{BT} of a particular fluid flow on a particular cylinder because it is the dominant phase.
3. The higher wall shear stress on the non-circular surfaces of the multi-faceted cylinder contributed to the optimum N_{BT} phase moving closer to the cylinder wall and decreasing the optimum N_{BT} phase region, consequently increasing the steady-state N_{BT} phase region.
4. The thermal augmentation on the multi-faceted cylinder is contributed by the non-circular surfaces in which the thermal boundary layer, T^* , is larger than the circular cylinder for all fluid flow. Alumina and Titania produce relatively more significant T^* than water on both cylinders.
5. In general, nanofluid produces higher HTC than water on both cylinders. Higher HTC is also produced by the multi-faceted than the circular cylinder. However, water produces higher HTC than Titania at $Re=2000$.
6. Nanofluid produces higher Nu than water on both cylinders. However, in terms of improvement in heat transfer relative to the water on the circular cylinder, water fluid flow shows a more significant and linear improvement than nanofluid.

CONFLICT OF INTEREST

The authors declare that they have no known competing financial interests or personal relationships that could have appeared to influence the work reported in this paper.

NOMENCLATURE

C_p	Specific heat capacity, [J/K.Kg]
D	Diameter, [mm]
D_B	Brownian motion coefficient
D_T	Thermophoresis coefficient
d_s	nanoparticle diameter, [mm]
H_{mf}	Height of the multi-faceted cylinder, [mm]
HTC	Heat transfer coefficient, [$W\ m^{-2}K^{-1}$]
k	thermal conductivity, [$W\ m^{-1}K^{-1}$]
k_B	Boltzmann constant, [$m^2.kg/s^2.K$]
N_{BT}	Ratio of Brownian motion to thermophoresis coefficients
Nu_{mf}	Nusselt number of multi-faceted cylinder = hH_{mf}/K
Nu_c	Nusselt number of circular cylinder = hD_c/K
Nu°	Normalized Nusselt number = Nu_{mf}/Nu_c
Nu°_{cw}	Normalized to Nusselt number of water on circular cylinder = Nu_{mf}/Nu_{cw}
P	Pressure, [Pa]
Re	Reynolds number
Q'	Heat flux, [$W\ m^{-2}$]
T	Temperature, [Celsius/Kelvin]
T_b	Bulk temperature, [Celsius/Kelvin]
T_w	Wall temperature, [Celsius/Kelvin]
T_i	Inlet temperature, [Celsius/Kelvin]
T^*	Non-dimensionalized temperature = $(T - T_{inlet}) / (T_{wall} - T_{inlet})$

T_{wall}^*	Non-dimensionalized wall temperature = $(T_{wall\ c} - T_{sat}) / (T_{wall\ MF} - T_{sat})$
T^*_{iso}	Non-dimensionalized isothermal temperature = T / T_{inlet}
V	Velocity, [$m\ s^{-1}$]
\mathbf{v}	Velocity vector, [$m\ s^{-1}$]
X°	Dimensionless film thickness, [mm]
Y	Height of the cylinder, [mm]
Y^*	y-dimensionless = y/Y
\bar{y}	Velocity normal to the cylinder wall
y	cylinder location based on distance from the top, [mm]

Greek

δ	Film thickness, [mm]
δ^*	Circular and multi-faceted dimension differences, [mm]
τ	Shear stress, [Pa]
μ	Dynamic viscosity, [Pa.s]
ρ	Density, [$kg\ m^{-3}$]
σ	Surface tension coefficient, [$N\ m^{-1}$]
Γ	Liquid load/mass flow rate per length, [$kg\ s^{-1}m^{-1}$]
φ / \emptyset	Nanofluid volume fraction
θ	Local temperature difference

Subscripts

1	Air phase
2	Water phase
nf	nanofluid
f	fluid
p	particle

REFERENCES

- Alkasasbeh, Hamzeh T., Mohammed Z. Swalmeh, Hebah G. Bani Saeed, Feras M. Al Faqih, and Adeeb G. Talafha. (2020), "Investigation on Cnts-Water and Human Blood Based Casson Nanofluid Flow over a Stretching Sheet under Impact of Magnetic Field." *Frontiers in Heat and Mass Transfer* **14**: 1–7.
<https://doi.org/10.5098/hmt.14.15>
- Amir. Fithry, Mohd, Yusoff M. Zamri, and A. Hassan Saiful H. (2021), "Fluid Film Characteristics over Horizontal Multi-Faceted Tube and the Augmentation of Thermal Performance." *Applied Thermal Engineering* **201** (PB): 117795.
<https://doi.org/10.1016/j.applthermaleng.2021.117795>
- Bock, Bradley D., Josua P. Meyer, and John R. Thome. (2019), "Falling Film Boiling and Pool Boiling on Plain Circular Tubes: Influence of Surface Roughness, Surface Material and Saturation Temperature on Heat Transfer and Dryout." *Experimental Thermal and Fluid Science* **109** (June): 109870.
<https://doi.org/10.1016/j.expthermflusci.2019.109870>
- Bock Choon Pak, Young. I. Cho. (2013), "Hydrodynamic and Heat Transfer Study of Dispersed Fluids With Submicron Metallic Oxide." *Experimental Heat Transfer: A Journal of, Thermal Energy Transport, Storage, and Conversion*, no. January 2013: 37–41.
<http://dx.doi.org/10.1080/08916159808946559>
- Brinkman, H. C. (1952), "The Viscosity of Concentrated Suspensions and Solutions." *The Journal of Chemical Physics* **20** (4): 571.
<https://doi.org/10.1063/1.1700493>
- Buongiorno, Jacopo. (2006), "Convective Transport in Nanofluids." *Journal of Heat Transfer* **128** (3): 240–50.
<https://doi.org/10.1115/1.2150834>
- Cheng, Ze, and Jie Peng. (2020), "Wavy Falling Film of Nanofluid over a Vertical Plate Considering Nanoparticle Migration." *International*

Journal of Heat and Mass Transfer **146**: 118895.
<https://doi.org/10.1016/j.ijheatmasstransfer.2019.118895>

Duangthongsuk, Weerapun, and Somchai Wongwises. (2008), "Effect of Thermophysical Properties Models on the Predicting of the Convective Heat Transfer Coefficient for Low Concentration Nanofluid." International Communications in Heat and Mass Transfer **35** (10): 1320–26.
<https://doi.org/10.1016/j.icheatmasstransfer.2008.07.015>

Eichinger, S., T. Storch, T. Grab, T. Fieback, and U. Gross. (2018), "Investigations of the Spreading of Falling Liquid Films in Inclined Tubes." International Journal of Heat and Mass Transfer **119**: 586–600.
<https://doi.org/10.1016/j.ijheatmasstransfer.2017.11.142>

Gao, Hongtao, Fei Mao, Yuchao Song, Jiaju Hong, and Yuying Yan. (2020), "Effect of Adding Copper Oxide Nanoparticles on the Mass/Heat Transfer in Falling Film Absorption." Applied Thermal Engineering **181** (March).
<https://doi.org/10.1016/j.applthermaleng.2020.115937>

Hamida, Mohamed Bechir Ben, Jalel Belghaieb, and Nejib Hajji. (2018), "Heat and Mass Transfer Enhancement for Falling Film Absorption Process in Vertical Plate Absorber by Adding Copper Nanoparticles." Arabian Journal for Science and Engineering **43** (9): 4991–5001.
<https://doi.org/10.1007/s13369-018-3252-9>

Hou, Hao, Qincheng Bi, Hong Ma, and Gang Wu. (2012), "Distribution Characteristics of Falling Film Thickness around a Horizontal Tube." Desalination **285**: 393–98.
<https://doi.org/10.1016/j.desal.2011.10.020>

Jani, Saeid. (2013), "Al₂O₃-Water Nanofluid Falling-Film Flow and Heat Transfer Characteristics on a Horizontal Circular Tube." Journal of Enhanced Heat Transfer **20** (3): 213–23.
<https://doi.org/10.1615/JEnhHeatTransf.2013007763>

Jin, Pu Hang, Zhuo Zhang, Ibrahim Mostafa, Chuang Yao Zhao, Wen Tao Ji, and Wen Quan Tao. (2019), "Heat Transfer Correlations of Refrigerant Falling Film Evaporation on a Single Horizontal Smooth Tube." International Journal of Heat and Mass Transfer **133**: 96–106.
<https://doi.org/10.1016/j.ijheatmasstransfer.2018.12.053>

Kang, Yong Tae, Hyun June Kim, and Kang Il Lee. (2008), "Heat and Mass Transfer Enhancement of Binary Nanofluids for H₂O/LiBr Falling Film Absorption Process." International Journal of Refrigeration **31** (5): 850–56.
<https://doi.org/10.1016/j.ijrefrig.2007.10.008>

Kim, Jin Kyeong, Jun Young Jung, and Yong Tae Kang. (2006), "The Effect of Nano-Particles on the Bubble Absorption Performance in a Binary Nanofluid." International Journal of Refrigeration **29** (1): 22–29.
<https://doi.org/10.1016/j.ijrefrig.2005.08.006>

Lee, Jin Ki. (2009), "The Effect of Additives and Nanoparticles on Falling Film Absorption Performance of Binary Nanofluids (H₂O/LiBr + Nanoparticles)." Journal of Nanoscience and Nanotechnology **9** (12): 7456–60.
<https://doi.org/10.1166/jnn.2009.1790>

Li, Yanjun, Kai Du, Huitao Hu, Liu Yang, and Shuhong Li. (2015) "Experimental Investigation on Enhancement of Ammonia-Water Falling Film Generation by Adding Carbon Black Nanoparticles." Experimental Thermal and Fluid Science **68**: 593–600.
<https://doi.org/10.1016/j.expthermflusci.2015.06.019>

Malvandi, A., D. D. Ganji, and I. Pop. (2016) "Laminar Filmwise Condensation of Nanofluids over a Vertical Plate Considering

Nanoparticles Migration." Applied Thermal Engineering **100**: 979–86.
<https://doi.org/10.1016/j.applthermaleng.2016.02.061>

Malvandi, A., Amirmahdi Ghasemi, D. D. Ganji, and I. Pop. (2016) "Effects of Nanoparticles Migration on Heat Transfer Enhancement at Film Condensation of Nanofluids over a Vertical Cylinder." Advanced Powder Technology **27** (5): 1941–48.
<https://doi.org/10.1016/j.apt.2016.06.025>

Oztop, Hakan F., and Eiyad Abu-Nada. (2008) "Numerical Study of Natural Convection in Partially Heated Rectangular Enclosures Filled with Nanofluids." International Journal of Heat and Fluid Flow **29** (5): 1326–36.
<https://doi.org/10.1016/j.ijheatfluidflow.2008.04.009>

Pang, Changwei, Weidong Wu, Wei Sheng, Hua Zhang, and Yong Tae Kang. (2012), "Mass Transfer Enhancement by Binary Nanofluids (NH₃/H₂O + Ag Nanoparticles) for Bubble Absorption Process." International Journal of Refrigeration **35** (8): 2240–47.
<https://doi.org/10.1016/j.ijrefrig.2012.08.006>

Parken, W. H., L. S. Fletcher, V. Sernas, and J. C. Han. (1990), "Heat Transfer through Falling Film Evaporation and Boiling on Horizontal Tubes." Journal of Heat Transfer **112** (3): 744–50.
<https://doi.org/10.1115/1.2910449>

Pu, Liang, Qiang Li, Xiangyu Shao, Lan Ding, and Yanzhong Li. (2019), "Effects of Tube Shape on Flow and Heat Transfer Characteristics in Falling Film Evaporation." Applied Thermal Engineering, 412–19.
<https://doi.org/10.1016/j.applthermaleng.2018.11.043>

Rashidi, Saman, Omid Mahian, and Ehsan Mohseni Languri. (2018), "Applications of Nanofluids in Condensing and Evaporating Systems: A Review." Journal of Thermal Analysis and Calorimetry **131** (3): 2027–39.
<https://doi.org/10.1007/s10973-017-6773-7>

Ruan, Binglu, and Anthony M. Jacobi. (2011), "Investigation on Intertube Falling-Film Heat Transfer and Mode Transitions of Aqueous-Alumina Nanofluids." Journal of Heat Transfer **133** (5): 1–11.
<https://doi.org/10.1115/1.4002980>

B. Ruan and A. Jacobi (2012). "Heat Transfer Characteristics of Multiwall Carbon Nanotube Suspensions (MWCNT Nanofluids) in Intertube Falling-Film Flow." International Journal of Heat and Mass Transfer **55** (11–12): 3186–95.
<https://doi.org/10.1016/j.ijheatmasstransfer.2012.02.051>

Ruan, Binglu, Anthony M. Jacobi, and Liansheng Li. (2010), "Heat Transfer of Falling Film Flowing around a Horizontal Tube with Nanofluids." Proceedings of the ASME Micro/Nanoscale Heat and Mass Transfer International Conference 2009, MNHMT2009 3: 643–52.
<https://doi.org/10.1115/MNHMT2009-18553>

Ruan, Jiagao, Jinping Liu, Xiongwen Xu, Jianxun Chen, and Guoli Li. (2018), "Experimental Study of an R290 Split-Type Air Conditioner Using a Falling Film Condenser." Applied Thermal Engineering **140**: 325–33.
<https://doi.org/10.1016/j.applthermaleng.2018.05.022>

Sharma, Lohit, Sunil Kumar, Robin Thakur, Bhaskar Goel, Amar Raj Singh Suri, Sashank Thapa, Nitin Kumar, Rajesh Maithani, and Anil Kumar. (2020), "A Review on Exergy Analysis of Nanofluid Flow through Several Conduits." Frontiers in Heat and Mass Transfer **14**: 1–15.
<https://doi.org/10.5098/hmt.14.30>

Singh, Yashwant, Rajesh Maithani, Sunil Kumar, Ehsan Gholamalazadeh, and Anil Kumar. (2018), "Development of New Correlations for Nusselt Number and Friction Factor of TiO₂/Water Based Nanofluid Flow in V-Pattern Protrusion Ribbed Square Channel." Frontiers in Heat and Mass

Transfer 11.

<https://doi.org/10.5098/hmt.11.33>.

Turkylmazoglu, Mustafa. (2015), “Analytical Solutions of Single and Multi-Phase Models for the Condensation of Nanofluid Film Flow and Heat Transfer.” *European Journal of Mechanics, B/Fluids* **53**: 272–77. <https://doi.org/10.1016/j.euromechflu.2015.06.004>.

Turkylmazoglu, Mustafa (2017), “Condensation of Laminar Film over Curved Vertical Walls Using Single and Two-Phase Nanofluid Models.” *European Journal of Mechanics, B/Fluids* **65**: 184–91. <https://doi.org/10.1016/j.euromechflu.2017.04.007>.

Wen, Tao, Lin Lu, and Hong Zhong. (2018), “Investigation on the Dehumidification Performance of LiCl/H₂O-MWNTs Nanofluid in a Falling Film Dehumidifier.” *Building and Environment* **139** (May): 8–16. <https://doi.org/10.1016/j.buildenv.2018.05.010>.

Wunder, Felix, Sabine Enders, and Raphael Semiat. (2017), “Numerical Simulation of Heat Transfer in a Horizontal Falling Film Evaporator of Multiple-Effect Distillation.” *Desalination* **401**: 206–29. <https://doi.org/10.1016/j.desal.2016.09.020>.

Xuana, Yimin, and Wilfried Roetzels. (2000), “Conceptions for Heat Transfer Correlation of Nanofluids.” *International Journal of Heat and Mass Transfer* **43** (19): 3701–7. [https://doi.org/https://doi.org/10.1016/S0017-9310\(99\)00369-5](https://doi.org/https://doi.org/10.1016/S0017-9310(99)00369-5).

Yang, Liu, Kai Du, Bo Cheng, and Yunfeng Jiang. (2010), “The Influence of Al₂O₃ Nanofluid on the Falling Film Absorption with Ammonia-Water.” *Asia-Pacific Power and Energy Engineering Conference, APPEEC*, no. **50876020**: 1–4. <https://doi.org/10.1109/APPEEC.2010.5449136>.

Yang, Liu, Kai Du, Xiao Feng Niu, Bo Cheng, and Yun Feng Jiang. (2011), “Experimental Study on Enhancement of Ammonia-Water Falling Film Absorption by Adding Nano-Particles.” *International Journal of Refrigeration* **34** (3): 640–47. <https://doi.org/10.1016/j.ijrefrig.2010.12.017>.

Yang, Liu, Kai Du, Xiaofeng Niu, Yuan Zhang, and Yanjun Li. (2014), “Numerical Investigation of Ammonia Falling Film Absorption Outside Vertical Tube with Nanofluids.” *International Journal of Heat and Mass Transfer* **79**: 241–50. <https://doi.org/10.1016/j.ijheatmasstransfer.2014.08.016>.

Zhang, L Y, Y Wang., Y. Liu, H. Q. Li, X. H. Yang, and L. W. Jin (2016), “Experimental Study on Enhanced Falling Film Absorption Process Using H₂O/LiBr Nanofluids.” *Proceedings of the ASME 2016 5th International Conference on Micro/Nanoscale Heat and Mass Transfer*, 1–8. <https://doi.org/10.1115/MNHMT2016-6630>

Zhang, Lianying, Zhibo Fu, Yuanyuan Liu, Liwen Jin, Qunli Zhang, and Wenju Hu. (2018), “Experimental Study on Enhancement of Falling Film Absorption Process by Adding Various Nanoparticles.” *International Communications in Heat and Mass Transfer* **92**: 100–106. <https://doi.org/10.1016/j.icheatmasstransfer.2018.02.011>.

Zhao, Chuang Yao, Wen Tao Ji, Ya Ling He, Ying Jie Zhong, and Wen Quan Tao. (2018), “A Comprehensive Numerical Study on the Subcooled Falling Film Heat Transfer on a Horizontal Smooth Tube.” *International Journal of Heat and Mass Transfer* **119**: 259–70. <https://doi.org/10.1016/j.ijheatmasstransfer.2017.11.077>.

Zhao, Chuang Yao, Wen Tao Ji, Pu Hang Jin, Ying Jie Zhong, and Wen Quan Tao. (2018), “Hydrodynamic Behaviors of the Falling Film Flow on a Horizontal Tube and Construction of New Film Thickness Correlation.” *International Journal of Heat and Mass Transfer* **119**: 564–76. <https://doi.org/10.1016/j.ijheatmasstransfer.2017.11.086>.

Zheng, Yi, Xuehu Ma, Yun Li, Rui Jiang, Kai Wang, Zhong Lan, and Qianqing Liang. (2017), “Experimental Study of Falling Film Evaporation Heat Transfer on Superhydrophilic Horizontal-Tubes at Low Spray Density.” *Applied Thermal Engineering* **111**: 1548–56. <https://doi.org/10.1016/j.applthermaleng.2016.07.177>.